A CMOS compatible platform for high impedance superconducting quantum circuits

Kazi Rafsanjani Amin, Carine Ladner, Guillaume Jourdan, Sebastien Hentz, Nicolas Roch, Julien Renard

A CMOS compatible platform for high impedance superconducting quantum circuits

Kazi Rafsanjani Amin,[1,2] Carine Ladner,[2] Guillaume Jourdan,[2] Sebastien Hentz,[2] Nicolas Roch,[1] and Julien Renard[1]

[1] *Univ. Grenoble Alpes, CNRS, Grenoble INP, Institut Neél, 38000 Grenoble, France*
[2] *Univ. Grenoble Alpes, CEA, LETI, 38000 Grenoble, France*

Aluminium based platforms have allowed to reach major milestones for superconducting quantum circuits. For the next generation of devices, materials that are able to maintain low microwave losses while providing new functionalities, such as large kinetic inductance or compatibility with CMOS platform are sought for. Here we report on a combined direct current (DC) and microwave investigation of titanium nitride films of different thicknesses grown using CMOS compatible methods. For microwave resonators made of TiN film of thickness ∼3 nm, we measured large kinetic inductance $L_K \sim 240$ pH/sq, high mode impedance of ~ 4.2 kΩ while maintaining microwave quality factor $\sim 10^5$ in the single photon limit. We present an in-depth study of the microwave loss mechanisms in these devices that indicates the importance of quasiparticles and provide insights for further improvement.

I. INTRODUCTION

After two decades of intense research, major developments have been made in quantum technologies. Superconducting circuits is one of the leading platform for quantum computing to date, with major milestone of computational advantage being reported recently[1, 2]. In this perspective, while fabrication of long-coherence quantum two-level systems is a hot pursuit, superconducting microwave devices comprising qubits and microwave resonators are already being used to study a wide variety of fundamental problems such as ultrastrong light-matter coupling [3, 4], many-body quantum physics [5, 6], quantum simulation of interactions in a lattice [7–9], or topological protection [10, 11]. For such studies, a prerequesite is the use of a material presenting a minimal amount of microwave losses. In addition, one of the building blocks for the recent developments of superconducting quantum circuits is a lossless, high inductance element, called superinductance [12]. Its impedance becomes comparable to the resistance quantum $R_Q = h/4e^2 \approx 6.5$ kΩ at microwave frequencies. This is a key feature to realize qubits that are protected from decoherence [13–15] or to enhance the coupling between a qubit and a microwave resonator [16, 17].

The superconducting quantum technologies have so far flurished using aluminium based technology that naturally provides a material with very low microwave losses and an excellent oxide for tunnel jonctions. In this platform superinductances have been achieved with large arrays of Al-AlO_X based Josephson junctions (JJ)s [18–20]. However, as the complexity of a real-life problem being addressed by a quantum processor increases, integration of a large number of qubits and resonators becomes inevitable. Developing suitable technology achieving scalablity of quantum devices for quantum computing is now seen as one of the next big challenge. For superinductances, current fabrication technology is incompatible with scalable platforms, and becomes increasingly challenging upon increasing the number of JJs in the array.

This has recently motivated the study of alternative new materials for fabrication of scalable superconducting quantum device. Several materials have been used to fabricate low losses microwave resonators and high-coherence qubits [21–23]. Fabrication of superinductances using kinetic inductance of disordered superconductor thin films became a promising alternative to Al, and different materials such as TiN [24–27], NbTiN [28], NbN [29, 30], AlO_x [21, 31, 32], InO_x [33, 34], doped Si [35], Tungsten [36] have been investigated. Amongst these materials, TiN and NbTiN have also been studied as substitutes of Al to fabricate low-loss microwave quantum circuits [24–27].

Microwave electrodynamics of disordered TiN [37, 38], as well as study of direct current (DC) resistivity have been reported in TiN and NbTiN. The effect of magnetic disorders on the superconducting behavior of TiN has also been studied [39]. Very high quality resonators, with internal quality factor at high electric field as large as 10^7 [25, 26] have been fabricated using thick films of TiN. In addition, NbTiN-based nanowire superinductances have been used to realize a fluxonium qubit [40].

Different deposition, film growth techniques [27, 41] and etch methods [39, 42] towards fabrication of microwave superconducting circuits have been investigated in details. However, with reducing thickness and increasing amount of disorder, the microwave losses and sample variability increase, compromising future integration in large scale devices. Hence, a detailed understanding of microwave loss mechanisms in these emerging materials is highly needed [43].

In this work we demonstrate TiN superconducting circuits fabricated with a VLSI, CMOS-compatible process featuring, at the same time high film quality, ultra-low microwave losses down to the quantum regime and high kinetic inductance. We study in details the microwave loss mechanisms in high kinetic inductance TiN film microwave resonators, and find that the quality factor of very-large kinetic inductance resonators might be limited by quasiparticles.

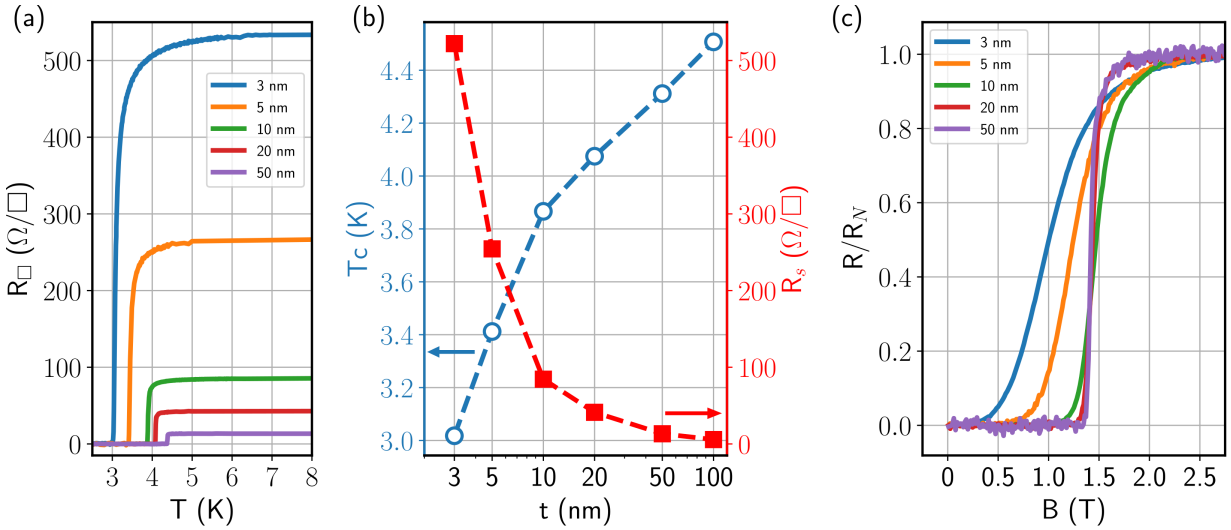

Figure 1: Superconducting transitions in TiN thin films. (a) Sheet resistance $R_\square$ versus temperature T for TiN films of different thicknesses t, zoomed in near the superconducting transitions. Data for 100 nm thin film is shown in Appendix-B, Fig. 11 for clarity. (b) T_C versus t, with blue open circles in left axis, and R_S versus t in red filled squares in right axis. The dashed lines are guides to the eye. (c) Normalized resistance versus perpendicular magnetic field B measured at $T = 2.0$ K for the same TiN film devices as presented in (a). Width of the superconducting to normal state transition increases with decreasing film thickness.

II. ORGANIZATION OF THIS MANUSCRIPT

We begin with presenting low frequency resistivity measurements from 300 K down to 1.9 K, and magnetic field 0-8 T. Film quality and superconductivity were characterized from the data. Measurement of 2D microstrip microwave resonators made out of 3, 5 and 10 nm thin TiN films are presented. Sheet kinetic inductance L_K were computed from both DC and microwave measurements, and their comparison is discussed. Then we investigate possible loss mechanisms of the thin TiN resonators. For this study, we use a 3D rectangular waveguide, and microstrip resonators are coupled to evanescent microwave fields inside the waveguide. Investigation of stability and aging of the microwave resonators are studied. Finally we discuss high impedance aspect of the microwave resonators. Details of the thin film deposition and resonator device fabrication are presented in details in Appendix-A.

III. RESULTS

Resistivity measurements

The TiN films of different thicknesses used in this work were deposited, using VLSI CMOS-compatible physical vapour deposition (PVD) method on high resistive, 725 μm thick intrinsic high-resistive silicon (100) wafer of 200 mm diameters. Excellent homogeniety and uniformity of film characteristics were achieved as a result of VLSI process. We first characterize the TiN thin films of different thicknesses by measuring sheet resistance $R_\square$ as a function of temperature T [Fig. 1(a)]. Starting from room temperature, when T decreases, $R_\square$ decreases first and then tends to reach a plateau for $T \lesssim 50$ K (see Appendix-B). Except for the 3 nm film, where the $R_\square$ increases with further cooling, $R_\square$ remains constant with T over a wide range upon further cooling, until the superconducting transitions are achieved. Such resistivity saturation below 50 K is a signature of disorders present in the films, and is similar to previous reports in TiN [44]. From these measurements, we extract the normal-state sheet resistance R_s [Fig. 1(b) right axis, in red filled squares], which is the value of $R_\square$ obtained just before the superconducting transition. R_S exhibits an increase by nearly two orders of magnitude as the film thickness reduces; from 5.7 Ω/□ observed for 100 nm film to 522.0 Ω/□ in 3 nm film. The residual-resistance ratios (RRR) calculated from the sheet resistance at room temperature $R_\square(300\ K)$ and R_s as $RRR = R_\square(300\ K)/R_s$ is a measure of disorder present in thin films and characterizes film quality. The largest value of RRR=1.3 observed for the 100 nm film is similar to RRR typically reported in high quality TiN thin films [44, 45]. We then obtain the superconducting transition temperature T_c [Fig. 1(b) left axis, blue open circles], defined as the temperature at which $R_\square$ drops below 1.0 % of R_s. The T_c decreases from 4.5 K measured for 100 nm film to 3.3 K for 3 nm film. Such decrease in T_C with decreasing film thickness is commonly observed in disordered thin film supercon-

ductors [46].

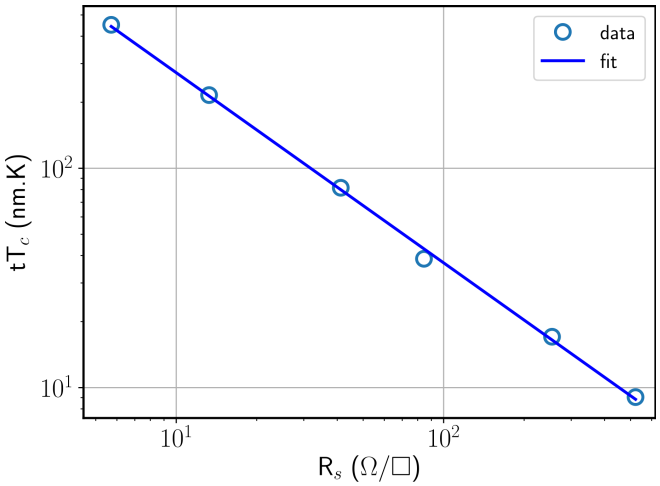

Figure 2: Universality and scaling of the superconducting transition in TiN thin films. The blue open circles are plots of tT_C versus R_S, in log-log scale. The blue line is fit to the data with $tT_c = AR_s^{-b}$, yielding the power-law exponent $b = 0.86 \pm 0.015$, very close to $b \approx 0.9 \sim 1.1$ widely observed in high-quality superconducting films[47].

In Fig. 1(c), we show plots of resistance versus perpendicular magnetic field B, measured at 2.0 K, for films of different thickness. The resistance values are normalized by the normal-state resistance obtained for each of these samples, measured above the critical magnetic field. The increase in resistance with increasing B signifies breakdown of superconductivity by introduction of vortices. For the thick films, *i.e.* the 20 nm and 50 nm films, the transition is rather sharp, with a critical magnetic field around 1.3 T, which is very large compared to critical magnetic field of standard superconductors, such as aluminum, traditionally used in superconducting quantum circuits. This suggests suitability of usage of TiN in fabricating quantum circuits where large magnetic field is required for device operation. In a type-II superconductor, magnetic field penetrates the sample beyond lower critical field H_{C1} and vortices are created. Movement of the vortices either because of electric field or because of thermal energy results into dissipation. In a disordered superconductor, vortices are pinned to defects and the zero-resistance state is maintained over a finite temperature range. Stronger pinning strength in thick films (in the 3D limit) allows larger magnetic field to penetrate the devices before dissipation sets in. In thin films near the 2D limit, however, much smaller magnetic field sets in dissipative electron transport [48].

Furthermore, we investigate the inter-dependence of T_C, R_S and film thickness t. A power-law $tT_c = AR_s^{-b}$ has been commonly observed in superconductors with different materials and disorder [47, 49]. With A being a material-dependent quantity, $b \approx 0.9 \sim 1.1$ has been observed to be an universal exponent for high-quality superconducting films [47]. A deviation points towards large granularity in the films. Fig. 2 shows a plot of tT_c versus R_s, extracted from measurements carried out with our TiN thin films (Fig. 1). While $b = 0.67$ was recently reported [27] for ALD-grown TiN films, we extract, from the fit, $b = 0.86 \pm 0.015$. This value is very close to the universality, and suggests a very high quality of our TiN thin films, even down to 3 nm thickness limit.

In Tbl. I, we summarize different characteristic parameters of our TiN thin films.

Table I: Thin film characteristics

Thickness (nm)	RRR	T_C (K)	R_S (Ω/□)	L_K (pH/□)
3	1.10	3.0	522.0	239.0
5	1.17	3.4	254.4	103.0
10	1.17	3.9	93.5	33.4
20	1.23	4.1	41.2	14.0
50	1.25	4.3	13.3	4.2
100	1.33	4.5	5.7	1.7

Microwave characterization

We begin microwave characterization with the study of 2D microstrip $\lambda/2$ resonators of different film thickness and different aspect ratio. We have studied a total 3 resonators made with 3 nm TiN film, 6 resonators made with 5 nm TiN film, and 5 resonators made with 10 nm TiN films. All the microwave measurements described below have been performed at the base temperature of the dilution refrigerator of 25 mK, unless otherwise specified. We obtain the coupling quality factor Q_C, internal quality factor Q_i and mode frequency f_R by fitting the data with standard fit procedures [50]. The average photon number n circulating in the resonator is estimated using $n = P_{in}Q_l^2/(\hbar\pi^2)f_R^2Q_C$, where P_{in} is the attenuated input power, and the loaded quality factor $Q_l^{-1} = Q_i^{-1} + Q_C^{-1}$. In Fig. 3(d-e), we show representative plots of S_{21} data, and fit to the data, obtained for a 5 nm thin film TiN resonator.

Kinetic inductance extraction

We now extract sheet kinetic inductance L_K of the films from both microwave measurements and low-

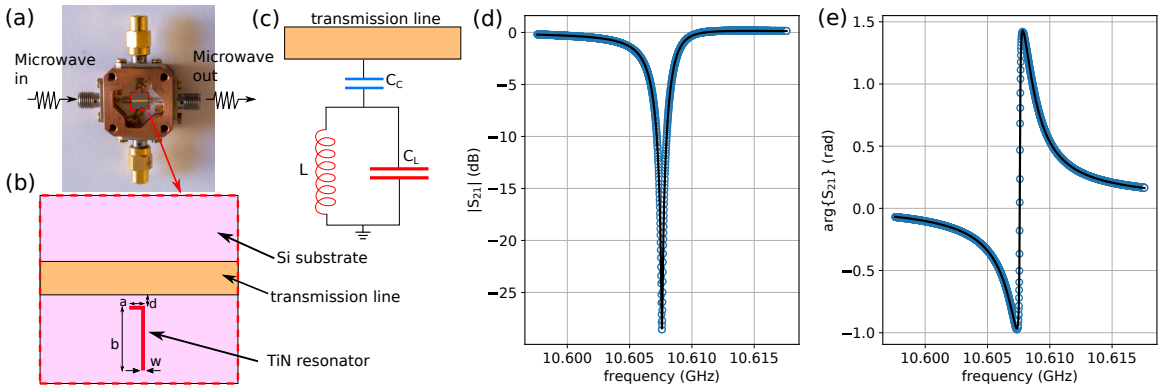

Figure 3: (a) Photograph of a custom-built copper sample holder, assembled with low-loss PCB and clamps to attach the sample chip, that allows microwave transmission measurements. Unused connectors are terminated with a matched impedance. (b) Schematic top view of a sample chip, showing an impedance matched microwave transmission line and a $\lambda/2$ TiN resonator (in red), capacitively coupled to the transmission line. (c) Lumped model of the microwave resonator. The inductance is obtained from L_K and the width w and length $l = a + b$ of the resonator. While C_L is the capacitance of the resonator obtained with the metallic ground plane at the bottom of the wafer, the coupling capacitance C_c is determined by dimensions of the coupling arm a and the separation from the transmission line d. Suitable coupling parameters are determined by FEM simulations using Sonnet®. (d-e) Transmission magnitude (d) and phase (e) of S_{21} showing a microwave resonance of 5 nm thick TiN resonator measured at 25 mK in 2D microstrip configuration. For this resonator, width $w = 500$ nm, $a = 125$ μm, $b = 375$ μm, and the separation $d = 200$ μm. In open circles, we plot S_{21} magnitude (d) and phase (e) data points, while the thick lines are the fit to the data. From the fits, we extract internal quality factor $Q_i \approx 1.16 \times 10^5$, and coupling quality factor $Q_c \approx 5000$ measured with $n \sim 5 \times 10^5$ circulating photons.

frequency resistivity measurements. We measure microwave resonators with length 6.5 mm and width of 2 μm, which, depending upon total inductance determined by L_K, exhibit multiple modes in our measurement bandwidth. In Fig. 4(a), we show plot of $|S_{21}|$ obtained for such a resonator made with 3 nm TiN film, showing 10 modes. In Fig. 4(b), we plot the mode frequencies, obtained from fit to the S_{21} data, versus mode index, for all 10 modes. We observe that the data points deviate progressively from the expected linear dispersion at higher frequencies as the effective plasma frequency is approached asymptotically. Furthermore, we fit the data using a modified version of long-range Coulomb interaction model [20], developed taking into account the charge screening by the presence of a ground plane at the back of the device chip [51], where total kinetic inductance is the only free parameter which we then extract from the measured dispersion..

Furthermore, we also perform a finite-element electromagnetic simulation using Sonnet®, and obtain resonant frequencies for our specific device geometry, and different values of sheet kinetic inductances L_K, which is an input parameter in the simulations. The experimentally obtained mode frequency is then used to fit into this simulated mode frequency versus L_K relationship, and estimate the kinetic inductance for out TiN films of a given thickness.

Sheet kinetic inductance, being directly proportional to the superfluid density of the superconducting film, is also obtained from low-frequency measurements of the superconducting transitions. We extract L_K of the films from the resistivity measurements [shown in Fig. 1] using the relationship $L_K = \hbar R_S/\pi\Delta_0$ [27, 28], where the zero temperature superconducting gap is obtained using the BCS relationship $\Delta_0 = 1.76 k_B T_C$. In Fig. 5 we combine L_K obtained from all the above mentioned measurements, for different film thicknesses. We observe excellent agreement in L_K between the three different methods, which gives high confidence in the extracted values. We emphasize here that all the DC and microwave measurements presented until now and to be discussed later for a given film thickness, are carried out from different parts of 200 mm diameter wafers. The agreement of L_K over all such measurements indicates excellent homogeneity of the stoichiometry and thickness, which is an asset of VLSI fabrication. For the 100 nm film, we obtain very small value of $L_K = 1.0$ pH/□, at the limit where L_K contributes negligibly to the total inductance. The L_K increases with decreasing thickness, reaching a significant value of 239 pH/□ (Tbl. I) for the 3 nm TiN film, two orders of magnitude larger than the value for 100 nm film. This increase in L_K with decrease in film thickness is a consequence of reduction of superfluid density in the superconducting state. Our observation of such an increase in the L_K with decreasing thickness is in qualitative agreement with TiN films deposited using other methods [27] and other disordered thin-film superconductors.

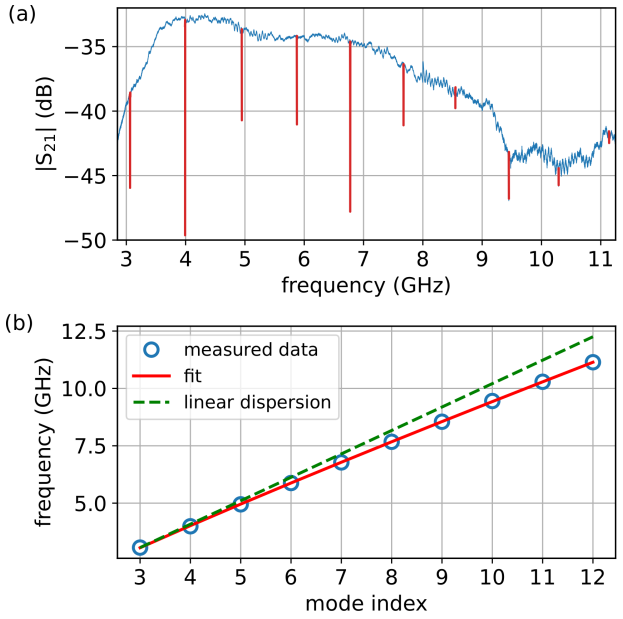

Figure 4: Mode dispersion in high kinetic impedance TiN microwave resonators. (a) Magnitude of microwave transmission parameter S_{21}(raw data) for a 3 nm thin film TiN resonator, fabricated in a microstrip configuration. 10 resonance modes were observed in the measurement bandwidth, and are plotted in red, for clarity. (b) Mode dispersion relation for the resonator, extracted from measurement shown in (a). The blue open circles are plots of mode frequency for different mode index. The green dashed line is the expected linear dispersion relation, obtained by fitting the data at low mode number. The red thick line is the fit to the data with the dispersion relation using long range Coulomb interaction model, that give L_K as the only fit parameter.

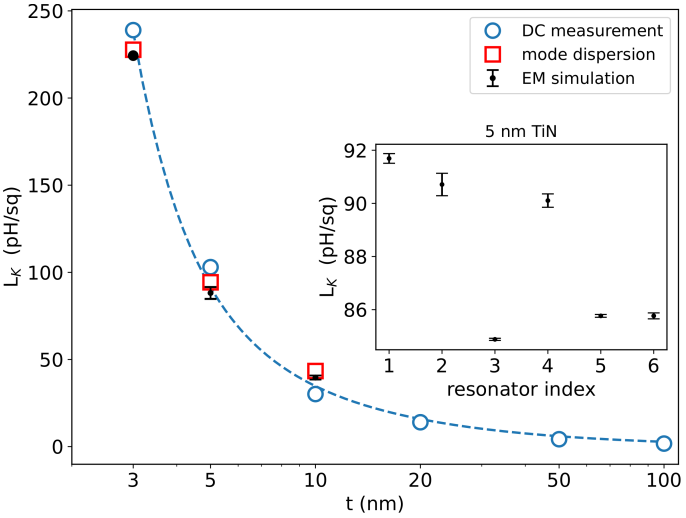

Figure 5: Kinetic inductance of TiN thin films. Plots of sheet kinetic inductance L_K versus TiN film thickness t, extracted using three different methods. The blue dashed line is a guide to the eye. L_K computed from superconducting transition temperature T_C and normal state sheet resistance R_s obtained just before superconducting transition, from resistance versus temperature measurements of TiN films of different thickness as $L_K = \hbar R_s/1.76\pi k_B T_C$ is plotted with blue open circles. L_K obtained from resonance frequency versus mode number dispersion relation for $\lambda/2$ microwave resonators in a microstrip configuration fabricated from 3, 5, 10 nm TiN films are shown with red open box. In black filled circles, we show plots of L_K obtained from electromagnetic simulation using Sonnet®, where L_K were tuned as a parameter of simulation to match mode frequency for a resonator of a given dimensions with experimentally obtained mode frequency. The errorbars represent spread in absolute value of the estimation from multiple resonators of different dimensions. Inset: Plot of L_K obtained using Sonnet simulations from 6 different microwave resonators, made with 5 nm TiN film, show a spread of less than 8% in L_K. The errorbars are estimated using resonance linewidth as an error estimate for resonance frequency of the observed resonance.

Investigation of microwave loss mechanisms

We now probe into the loss mechanisms, that determine the intrinsic performances of the TiN microwave resonators. A very common source of loss in microwave resonators and other superconducting quantum devices are two-level systems (TLS) [52] which are present in the vicinity of the devices and coupled to them. A series of detailed investigations showed that impurities residing in the metal-substrate interface is the major contributor to the TLS loss. This can be attributed to the order of magnitude larger participation of stored electric field in metal-substrate interfaces, as compared to metal-air or substrate-air interfaces [52]. On the other hand, as the kinetic inductance fraction $\alpha = L_{kinetic}/L_{total}$ approaches unity, susceptibility to quasiparticles (QP), and in turn, induced microwave losses due to QP increases [31, 53]. Non-equilibrium quasiparticles in high kinetic inductance granular aluminum resonators have been found to be the dominant source of microwave loss [31, 54, 55]. We study the evolution of internal quality factors of multiple TiN resonators, both in planar microstrip geometry and in rectangular 3D waveguide, with variation of microwave power and temperature to unravel the underlying loss mechanisms.

We study multiple microstrip version of $\lambda/2$ resonators, embedded into a 3D rectangular copper waveguide similar to that in ref. [31]. An impedance-matched wave port is used to excite the resonator. With the help of finite element simulations using the *Ansys© HFSS* software, we chose the dimensions of the resonators, in order to achieve a coupling quality factor Q_c in the range $10^5 - 10^6$ and the frequency in range of 4.0 − 6.0 GHz, below the passband of the waveguide. We couple the resonators with the evanescent wave of the waveguide in order to achieve Q_c within an order of magnitude of Q_i to have good

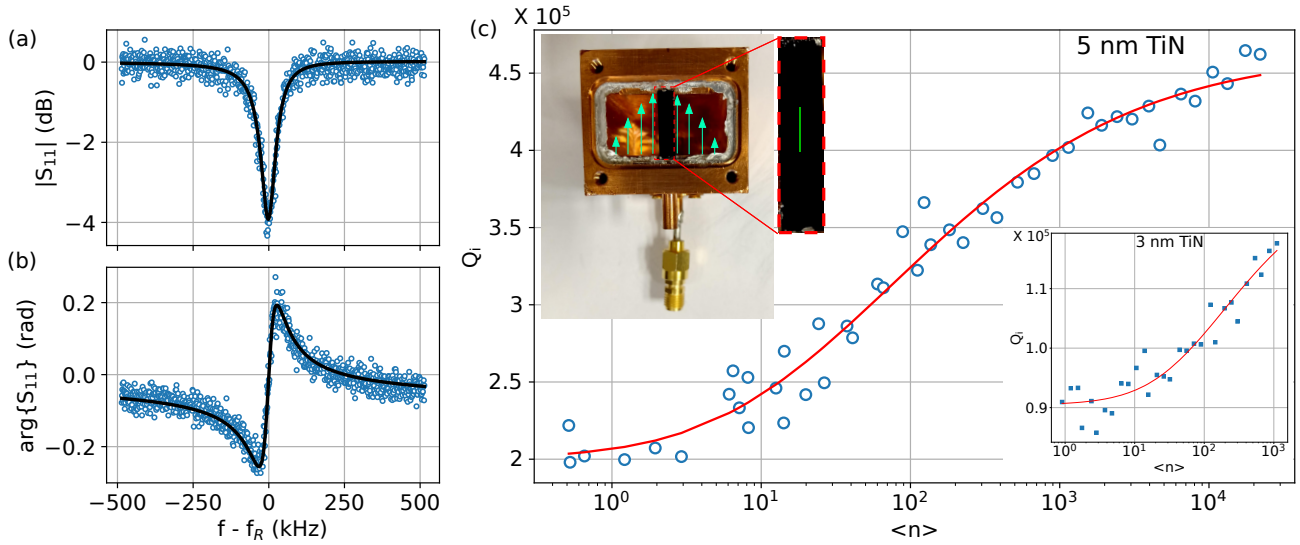

Figure 6: Photon number dependent microwave losses in TiN thin films resonators. Plots of (a) magnitude and (b) phase of S_{11} parameter of a 3 nm thick film TiN resonator, with $f_R = 5.563$ GHz measured using a 3D waveguide, shown in left-top inset of (c), with single circulating photon in the resonator. The blue open circles are data points while the black lines are the fit to the data points [50]. We extract $Q_i = 0.9 \times 10^5$, $Q_c = 4.1 \times 10^5$ and $< n >= 1.3$ from the fits. (c) Plots of Q_i versus average number of photons n measured for a 5 nm thick film TiN resonator. The blue open circles are the data points while the red lines are fit to the data points using QP (Eqn. 1) induced loss model. Left-top inset: Optical image of the copper 3D waveguide used in the experiments. A $\lambda/2$ resonator is represented (not to scale) in the silicon chip, shown magnified in the right. The electric field magnitude of the fundamental TE_{10} mode is represented by arrows. Right-bottom inset: Plots of Q_i versus n measured for a 3 nm thick film TiN resonator (blue open circles), and fit to the data points, similar to that shown in the main panel.

confidence in the fit procedure [50]. In Fig. 6, we show representative plots of magnitude (Fig. 6(a)) and phase of (Fig. 6(b)) S_{11}, for a 3 nm TiN resonator. The blue open circles are the data points, while the thick black lines are the fit to the data. From the fit, we obtain $Q_i \sim 0.9 \times 10^5$, measured in the single photon limit. Internal quality factor of $\sim 10^5$ in the single photon limit for such a thin film ($\sim$ 3 nm) high kinetic inductance resonator is comparable to the best values reported thus far [27, 31, 54–56].

Table II: Fit parameters for the data dispalyed in Fig 6(c)

parameter	3 nm TiN	5 nm TiN
Q_0	90442 ±997	200072 ± 6361
β	3.29×10^{-6}	2.85×10^{-6}
γ	0.011	0.063

We now present additional experiments to understand different loss mechanisms in the TiN resonators. First, we measure resonance traces for a wide range of input powers to extract Q_i as a function of photon number. In Fig. 6(c) we show, in blue open circles, plot of Q_i versus average number of circulating photons n in the resonator, measured for a 5 nm thick TiN resonator. We observe $Q_i \sim 2.0 \times 10^5$ in the single photon limit. We could measure the mode with up to $\sim$ 2×10^4 photons before the resonance mode bifurcates because of the intrinsic nonlinearity of TiN. Q_i increases from single photon limit by $\sim$ 2 times to $\sim$ 4.5 $\times 10^5$ and tends to saturate before bifurcation, over four orders of magnitude increase in the photon number. In the inset of Fig. 6(c), we show plots of Q_i versus n, measured for a resonator made with 3 nm thick TiN. We observe here a distinct behaviour for the Q_i versus n as compared to the 5 nm thick resonator. Firstly, the bifurcation onsets at $\sim 10^3$ photons in the resonator, almost an order of magnitude smaller than that in the 5 nm resonator. This can be attributed to larger Kerr nonlinearity arising because of larger L_K. Moreover, for 3 nm TiN, we observe $Q_i \sim 0.9 \times 10^5$ in the single photon limit, which indicates larger loss in the 3 nm resonators as compared to 5 nm TiN resonators. Over the three orders of magnitude increase in n, Q_i shows only a weak dependence on n for the 3 nm thick resonator. Such larger losses in 3 nm resonator as compared to 5 nm resonator have been consistently observed over multiple planar 2D microstrip resonators with different aspect ratios and frequencies, while the substrate and the entire fabrication procedure are same.

To gain more insight on the origin of loss mechanisms, in Fig. 7, we combine Q_i versus metal-substrate inter-

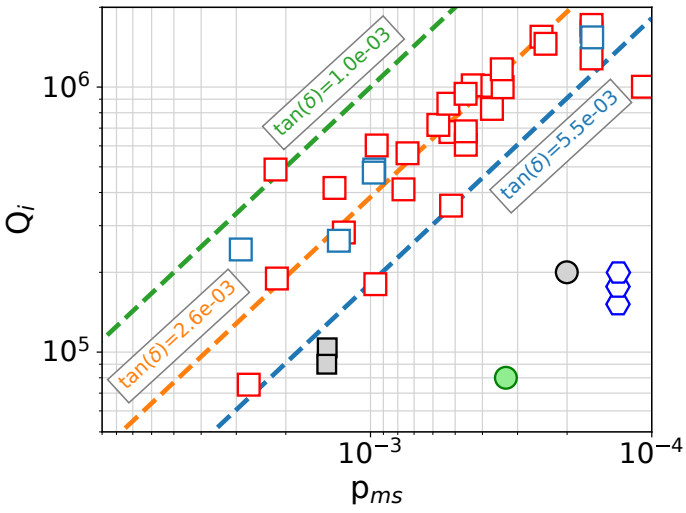

Figure 7: Internal quality factor versus metal-substrate participation ratio. The open squares represent characteristics of superconducting microwave resonators and transmon qubits from literature [red squares from Ref. [57] and blue squares from Ref. [31]]. Open pentagons represent high kinetic inductance GrAl microwave resonators [31], where Q_i were limited by quasiparticle loss. Data points from microwave resonators used in this work are represented by black (5 nm TiN) and green (3 nm TiN) filled squares and circles. The black filled squares correspond to Q_i of resonator measured in 2D microstrip configuration, while black filled circle recpresent Q_i of resonator measured using rectangular 3D waveguide. The dashed lines represent $Q_i = [p_{ms} \tan\delta]^{-1}$ for three different values of dielectric loss tangent $\tan\delta$, in range with typically measured values for high quality Si or sapphire substrates [31, 57–59].

face participation ratio p_{ms} obtained for our TiN resonators (filled circles and squares) and also from literature survey of resonators (open squares and pentagons), and transmon qubits dominated by capacitive losses. We obtain p_{ms} for our resonators by computing the fraction of energy stored in a 3 nm thick region under the resonator, following the standard methodology described in Ref. [57–59]. Q_i in the single photon limit, determined solely by dielectric loss in substrate scales as $Q_i = [p_{ms} \tan\delta]^{-1}$. We can identify two distinct types of data points. A cluster of data points from literature (open squares), for which the dominant loss is from two-level systems at metal substrate interface, obey the empirical relation $Q_i = [p_{ms} \tan\delta]^{-1}$. We observe a contrasting behaviour for TiN resonators measured in 3D waveguide. In a 3D rectangular waveguide, the ground plane is provided by the metal body of the waveguide, which in turn significantly reduces metal-substrate participation ratio by diluting the electric field in the substrate. However, we observe that the measured Q_i is limited to $\sim 10^5$, one order of magnitude less that that predicted by $Q_i = [p_{ms} \tan\delta]^{-1}$ for standard high-quality Si substrates. Similar suppression of Q_i by order of magnitude compared to what is predicted by $[p_{ms} \tan\delta]^{-1}$ were observed in high kinetic inductance GrAl resonators measured in similar 3D waveguides (open pentagons). Here the losses were found to be dominated by quasiparticle [31]. Q_i in 2D microstrip TiN resonator (black filled square), with p_{ms} orders of magnitude larger than that obtained in 3D waveguides, indeed match well with predicted value with $\tan\delta \sim 5.5 \times 10^{-3}$. We emphasis here that all of these resonators for a given film thickness are fabricated from the same 200 mm wafer of TiN films on Si, following the same fabrication recipe. For large p_{ms} ($\geq 10^{-3}$, [black filled squares]) the dominant loss is naturally from TLS at metal-surface interface, as any other loss mechanisms are masked off. On the other hand, as the p_{ms} is reduced for the TiN resonators measured in 3D waveguide [filled circles], larger suppression of Q_i than predicted by $Q_i = [p_{ms} \tan\delta]^{-1}$ clearly suggests that loss mechanisms other than TLS become progressively dominant for high kinetic inductance TiN resonators.

We now analyze our data with the model of photon number-dependent loss due to localized QP [31]:

$$\frac{1}{Q_i} = \frac{1}{Q_0} + \beta\left(\frac{1}{1+\frac{\gamma n}{1+\frac{1}{2}\sqrt{1+4\gamma n}-1}} - 1\right), \qquad (1)$$

with Q_0 being quality factor characterizing other loss mechanisms independent of n, and β quantifies QP-photon coupling strength. The red thick lines in Fig. 6(c) are the fit to the data points with Eqn. 1. We obtain a good agreement between the measured data and QP induced loss model, which suggests that QP induced losses are probably the dominant loss mechanism in our resonators, similar to previous observations in high kinetic inductance resonators [31, 55, 60]. QP can be generated in these devices because of photons, phonons or other high-energy particles, and often manifest as sudden frequency jumps of the resonators by 'bursts' of quasiparticles. However, identifying the exact origin of these QP is an active field of research, and beyond the scope of this work. We present the fit results in Tbl. II.

We now study dependence of Q_i on temperature T, by controlled heating of the mixing chamber, in a subsequent cooldown. In Fig. 8, we show plots of Q_i versus T, measured for 5 nm TiN (top panel) and 3 nm TiN (bottom panel). Q_i is essentially temperature independent until about 400 mK, and then decreases monotonously, but sharply with further increasing T. As temperature increases, the thermal equilibrium quasiparticle density n_{qp} increases [61, 62], as given by $n_{qp}(T) = D(E_F)\sqrt{2\pi k_B T \Delta}\exp(\Delta_0/k_B T)$, where $D(E_F)$ is the density of states at the Fermi energy, and Δ_0 is the zero temperature superconducting gap. The increasing n_{qp} results in additional loss in microwave resonators,

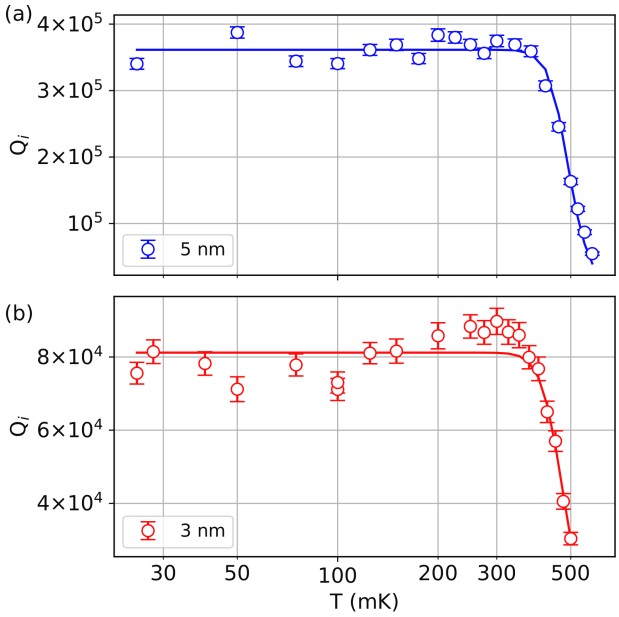

Figure 8: Temperature dependence of losses in TiN microwave resonators. Plots of Q_i versus T measured for (a) 5 nm (b) and 3 nm thick TiN resonator. The thick lines are fit to the data using Eqn. 2, which determine the loss of microwave resonators governed by increase in thermal quasiparticle density as T increases.

governed by:

$$\frac{1}{Qi} = 2\alpha\sqrt{\frac{k_B T}{\pi h f_R}}\exp\left(-\frac{\Delta_0}{k_B T}\right) + \frac{1}{Q_a} \qquad (2)$$

with $\alpha = L_{kinetic}/L_{total}$ being the kinetic inductance fraction, and $\frac{1}{Q_a}$ is loss because of other loss mechanisms, which, in our case, is dominated by loss due to non equilibrium localized QP, as discussed previously. The thick lines in Fig. 8 show the fit to the data using Eqn. 2, with only one free parameter Δ_0, and $\alpha = 1$. The estimated value of Δ_0 obtained from the fits agrees well, within 10% uncertainty [27, 63], with the BCS prediction of $1.76 k_B T_C$. We note here that, observed saturation in Q_i for $T \leq 400$ mK is contrasting to TLS predictions, where saturation of TLS because of provided thermal energy results in an increase in Q_i. Hence the measured temperature dependance of Q_i is in agreement with the previous discussion suggesting that the microwave loss in the single photon limit in TiN resonators in 3D waveguide is not predominantly TLS limited. Our results and interpretations inspire further investigation of the microwave loss mechanism in thin-film high kinetic inductance TiN resonators.

Thin film stability

A very important aspect for future integration and use in large scale circuits is device stability. At present, superconducting quantum devices, made with conventional Al-AlO_x-Al Josephson junctions suffer from a major drawback, which is aging of the Josephson junction. With time, characteristics of the materials alter, resulting in degradation of the device quality. These aging effects are often attributed to oxidation of the superconducting building block. Aging was also observed in the thinnest ALD TiN films reported in [27]. We investigate this aspect in our TiN films. We carry out multiple measurements of superconducting transitions in TiN thin films with a time gap of more that two months, and do not observe, within the measurement uncertainty, any change in the T_C or the sheet resistance. Furthermore, we study shift in resonance frequency or quality factors in TiN microwave resonators over a period of nearly three months, and do not observe any significant aging in our devices. In Fig. 9(a) we show plots of $|S_{21}|$ measured in one of our resonators made with 3 nm thin TiN film initially, and measured after three months. We observe a decrease in resonant frequency by only ∼20 MHz, which is a less than 1 % change, and is often observed in different cooldowns, while any significant oxidation would have resulted in an increase in L_K and an appreciable change in f_R. We also do not observe any significant change in the Q_i of the device, extracted from the resonances, over this time period. The devices were stored in ambient atmosphere inside a clean-room for the entire period of time. We note here that the first measurement were carried out after a couple of weeks of the film deposition, and we cannot rule out that a fast aging happens faster than this time scale. Nevertheless our experiments demonstrate long term stability which is the key feature sought for.

A large variety of device architecture used in modern quantum technology often require exposure of the devices to HF for removal of oxides [64, 65]. While it has been reported that the quality of relatively thicker devices improve, because of removal of native oxide from device surface, after exposure to HF for a very short amount of time [65], we investigate the robustness of very thin film microwave resonators under HF exposure for significantly longer time. We expose the thin film resonators with both liquid and vapour HF for sufficient long time, often equivalent to removal of 1 μm thermal silicon oxide, and observe only negligible alteration of the device quality, both in terms of resonant frequency and internal quality factors, suggesting extreme robustness of the thin films. In Fig. 9(b), we show representative plot of normalized $|S_{21}|$ of a 5 nm thick TiN resonator before and after exposure to HF. We also examine the device surface with high-resolution SEM, and observe that the

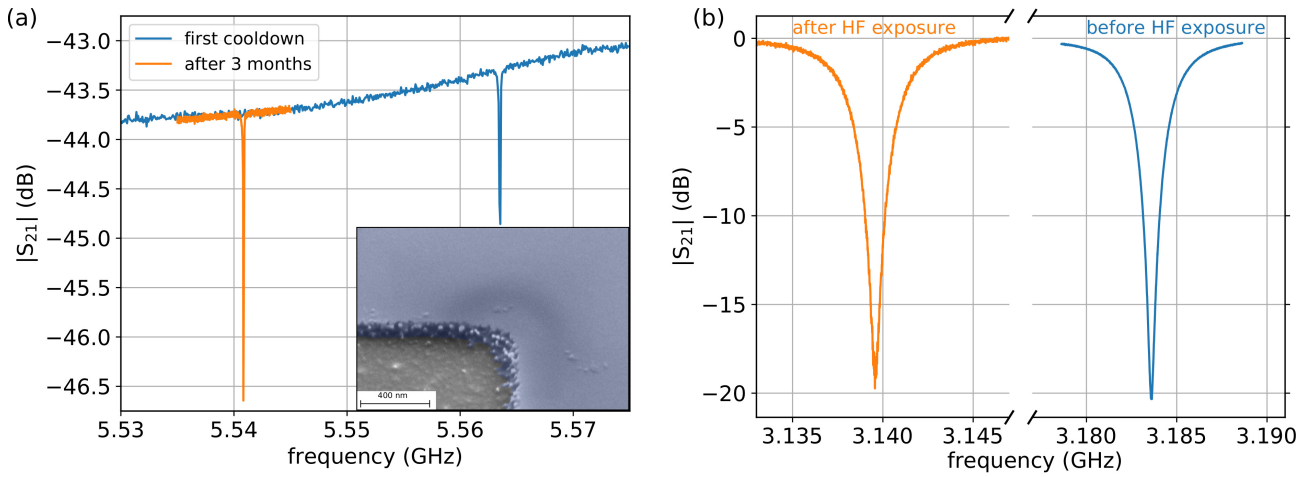

Figure 9: Stability of the TiN thin film resonators. (a) Plots of microwave transmission parameter $|S_{21}|$ for a 3 nm thick TiN resonator, measured with a gap of three months. Less that 1.0% reduction in the resonance frequency indicates only negligible aging affect in the resonator. (b) Plot of $|S_{21}|$ versus frequency for a 5 nm thick TiN resonator before and after exposure with HF. After the first measurement, the device was exposed to vapour HF of 4 steps of 300 s each, with an etch rate of 48 nm/min for thermal silicon oxide. Very small change in resonance frequency($\sim 1.5\%$) and Q_i suggest excellent robustness of the films under HF treatment. False color high resolution SEM image of a device after exposure to HF is shown in inset of (a).

surface quality is maintained after such HF exposures (inset of Fig. 9(a)). The stability of the device under such extreme condition opens up the possibility to integrate such devices with SOI wafers, commonly used in different device architectures. The very high quality and robustness of the grown TiN films make them a very suitable candidate to fabricate building blocks of superconducting quantum devices.

Impedance of the resonators

The total kinetic inductance of a superinductor of length l and width w can be estimated as $L_{kinetic} = \frac{l}{w} L_K = \frac{\hbar}{1.76\pi k_B} \frac{l}{w} \frac{R_N}{T_C}$, whereas, in the limit of $l \gg w \gg t$, t being the thickness, the geometric inductance can be approximated to $L_{geo} \approx \frac{\mu_0}{2\pi} l \ln(\frac{2l}{w})$ [60, 66]. For our 3 nm thick TiN resonator (Fig. 6), we obtain the kinetic inductance of the resonator $L_{kin} = 290$ nH. This value is comparable to the kinetic inductance of typical ~ 100 nH of high-impedance superinductors used in high-coherence fluxonium qubits [13, 21, 40, 67]. We also obtain $\alpha = 0.98$ and $\alpha = 0.99$ for 5 nm and 3 nm thick TiN resonators, respectively. Hence the constraints $\alpha = 1$ in the fit in Fig. 8 are well justified. Such large kinetic inductance, or equivalently $\alpha \sim 1$, is an approach towards obtaining high characteristic impedance. We estimate mode impedance $Z_c = \sqrt{\mathcal{L}/c}$, where $\mathcal{L}$ and c are inductance and capacitance per unit length of the resonator, of 3.2 kΩ for our 3 nm TiN resonator, measured in the 3D waveguide. We measure impedance as high as 4.2 kΩ for a 3 nm thick TiN resonator with mode frequency of 8.7 GHz in a 2D geometry. This mode impedance can be further modulated by modifying length and width of the resonator. While reduction of width increases the mode impedance, the Q_i were often observed to suffer from different loss mechanisms [29].

IV. CONCLUSIONS

In summary, we studied the microwave properties of superconducting TiN thin films fabricated with a VLSI platform. We showed that the films remain superconducting down to at least 3 nm, with a critical temperature still exceeding 3 K. When reducing the film thickness, the kinetic inductance increases up to 239 pH/□ for a 3 nm thick film. In microwave resonators, we demonstrate very large total inductance of several hundreds of nH and characteristic impedance $Z \approx 4.2$ kΩ together with state-of-the-art losses in the single photon regime, i.e. internal quality factors $Q_i \approx 10^5$. We show evidence that the remaining losses can be attributed to non-equilibrium quasiparticles. Mitigation strategies, such as an improved shielding or phonon traps might help to reduce the losses even further in the future. Our TiN showed negligible degradation due to aging, contrary to what is often observed in very thin films, and can withstand extended exposition to HF. All these demonstrations open up the possibility to develop industrial scale fabrication of superconducting microwave circuits. The compatibility of TiN with large magnetic field will also allow to integrate it into hybrid circuits using semiconductor spins and superconducting circuits.

V. ACKNOWLEDGMENT

This work was supported by the French National Research Agency (ANR) in the framework of the Graphmon project (ANR-19-CE47-0007) and the QNEMS project from LETI Carnot Institute. JR acknowledges F. Balestro, V. Bouchiat, E. Eyraud and W. Wernsdorfer for help with the cryogenic system. KRA acknowledge help of F. Faroughi in EM simulations and with 3D waveguide. We acknowledge the help of P. Lachkar for DC resistivity measurements. We acknowledge the work of J. Jarreau and L. Del-Rey for the fabrication of the 3D waveguide. We acknowledge support from the Nanofab team of Institut Néel, and from Guillaume Rodriguez of CEA Leti.

APPENDIX A: METHODS

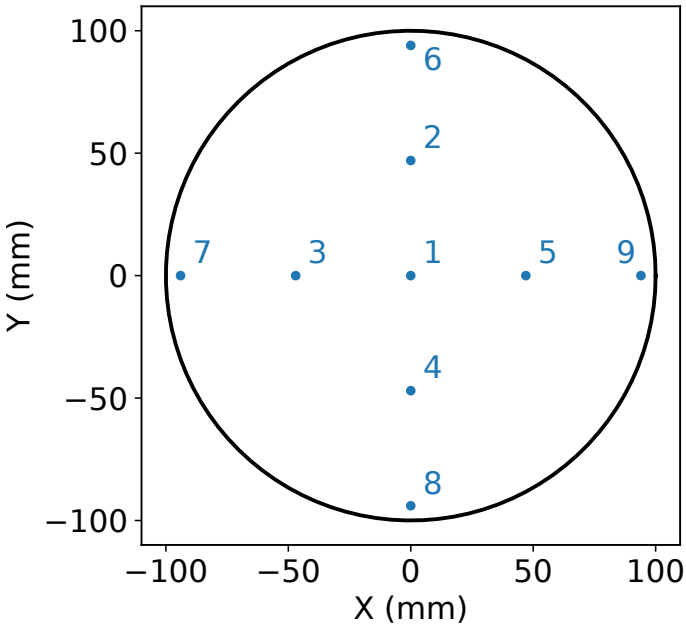

Figure 10: Measurement of thickness of TiN film by ellipsometry. The black circle represents outline of the silicon wafer of 200 mm diameter, with 10 nm TiN. The blue dots represent the positions where the film thicknesses were measured by ellipsometry. The measured values yield an average thickness of 10.6 nm, and a spread of 1.2 nm. The values are given in Tbl. III.

TiN thin films of six different thicknesses were deposited with a VLSI, CMOS-compatible physical vapour deposition (PVD) method at 350°C on high resistive, 725 μm thick intrinsic high-resistive silicon (100) wafer of 200 mm diameters. The thicknesses and film uniformity were characterized using ellipsometry and sheet resistance measurements using a probe-station. Both measurements were carried out at 9 different positions spread over the wafers [Fig 10], and suggested excellent homogeneity of the films. For a film of thickness targeted 10 nm, measured values from elipsometry yield an average thickness of 10.6 nm, and a spread of only 1.2 nm over the 200 mm diameter wafer. The values are given in Tbl. III. Resistivity measurements from 300 K down to 1.9 K, and magnetic field 0-8 T were then performed in a Physical Property Measurement Systems (PPMS), by a standard low-frequency a.c. four-probe method, with bias current kept sufficiently low to avoid Joule heating effect. Ti-Au ohmic current and voltage contact pads were deposited on the samples by electron beam evaporation. Microwave resonators were patterned by negative electron-beam lithography followed by SF_6 based dry-etching of the TiN [39]. Microwave $\lambda/2$ resonators, in a 2D microstrip configuration, were capacitively coupled to low-loss impedance matched transmission lines. The coupling was optimized with aid of EM simulations. Transmission line, and ground plane at the backside of the wafers were deposited using electron-beam evaporation. The device chips were wire-bonded to a custom-built high-frequency copper-made sample holder. Separately, microstrip $\lambda/2$ resonators were measured using a rectangular copper 3D waveguide, where the copper waveguide determines the ground, and provides a low-loss, clean microwave environment free of lossy components in close proximity to the resonator [68]. Microwave resonators were measured in a dilution refrigerator, with a base temperature of 25 mK.

Table III: Measurement of film thickness using ellipsometry. X and Y are the coordinates of the position where the measurements were taken.

Sl. No.	X (mm)	Y (mm)	thicnkess (nm)
1	0	0	10.96
2	0	47	11.28
3	-47	0	11.2
4	0	-47	11.2
5	47	0	11.17
6	0	94	10.13
7	-94	0	10.08
8	0	-94	10.11
9	94	0	10.12

APPENDIX B: ADDITIONAL PLOTS OF RESISTIVITY MEASUREMENTS

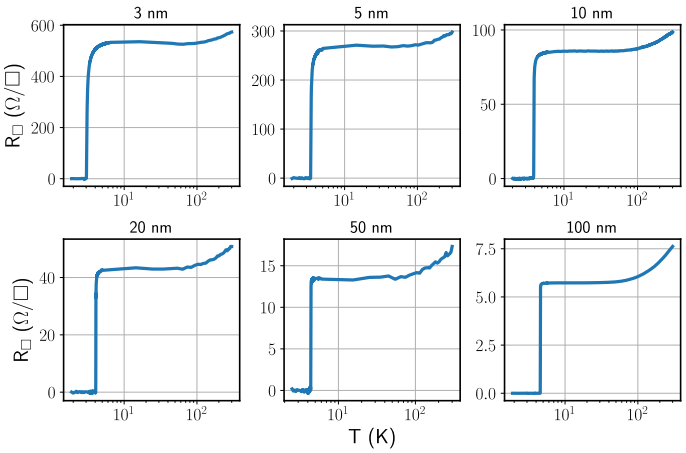

Figure 11: Temperature dependance of sheet resistance for TiN films of different thickness, from room temperature down to 1.9 K. Plots of the data zoomed in near the superconducting transitions are shown in Fig. 1.

APPENDIX C: IMPEDANCE OF THE MICROWAVE RESONATORS

The mode impedance of a microwave resonator is given by $Z_c = \sqrt{\mathcal{L}/c}$, where $\mathcal{L}$ and c are inductance and capacitance per unit length of the resonator. $\mathcal{L}$ for a microwave resonator of length l and width w can be approximated from L_K, in the limit of kinetic inductance fraction $\alpha = 1$ as $\mathcal{L} = L_K/w$ [29]. Equating the phase velocity $v_p = \dfrac{2\pi f_R}{k} = \dfrac{1}{\sqrt{\mathcal{L}c}}$, we can estimate the mode impedance from $Z_c = 2 f_r L_K(\frac{l}{w})$. In Tbl. IV, we summarize mode impedance of multiple $\lambda/2$ resonators of different thickness.

Table IV: Mode impedance of TiN resonators.

Sl. No.	f_R (GHz)	t (nm)	l (μm)	w (μm)	Z_c (kΩ)
1	8.69	3	300	0.3	4.15
2	5.57	3	600	0.5	3.19
3	10.6	5	500	0.5	2.18
4	3.93	5	2000	1.0	1.62

[1] F. Arute, K. Arya, R. Babbush, D. Bacon, J. C. Bardin, R. Barends, R. Biswas, S. Boixo, F. G. S. L. Brandao, D. A. Buell, B. Burkett, Y. Chen, Z. Chen, B. Chiaro, R. Collins, W. Courtney, A. Dunsworth, E. Farhi, B. Foxen, A. Fowler, C. Gidney, M. Giustina, R. Graff, K. Guerin, S. Habegger, M. P. Harrigan, M. J. Hartmann, A. Ho, M. Hoffmann, T. Huang, T. S. Humble, S. V. Isakov, E. Jeffrey, Z. Jiang, D. Kafri, K. Kechedzhi, J. Kelly, P. V. Klimov, S. Knysh, A. Korotkov, F. Kostritsa, D. Landhuis, M. Lindmark, E. Lucero, D. Lyakh, S. Mandrà, J. R. McClean, M. McEwen, A. Megrant, X. Mi, K. Michielsen, M. Mohseni, J. Mutus, O. Naaman, M. Neeley, C. Neill, M. Y. Niu, E. Ostby, A. Petukhov, J. C. Platt, C. Quintana, E. G. Rieffel, P. Roushan, N. C. Rubin, D. Sank, K. J. Satzinger, V. Smelyanskiy, K. J. Sung, M. D. Trevithick, A. Vainsencher, B. Villalonga, T. White, Z. J. Yao, P. Yeh, A. Zalcman, H. Neven, and J. M. Martinis, Quantum supremacy using a programmable superconducting processor, Nature **574**, 505 (2019).

[2] Y. Wu, W.-S. Bao, S. Cao, F. Chen, M.-C. Chen, X. Chen, T.-H. Chung, H. Deng, Y. Du, D. Fan, M. Gong, C. Guo, C. Guo, S. Guo, L. Han, L. Hong, H.-L. Huang, Y.-H. Huo, L. Li, N. Li, S. Li, Y. Li, F. Liang, C. Lin, J. Lin, H. Qian, D. Qiao, H. Rong, H. Su, L. Sun, L. Wang, S. Wang, D. Wu, Y. Xu, K. Yan, W. Yang, Y. Yang, Y. Ye, J. Yin, C. Ying, J. Yu, C. Zha, C. Zhang, H. Zhang, K. Zhang, Y. Zhang, H. Zhao, Y. Zhao, L. Zhou, Q. Zhu, C.-Y. Lu, C.-Z. Peng, X. Zhu, and J.-W. Pan, Strong quantum computational advantage using a superconducting quantum processor (2021), arXiv:2106.14734 [quant-ph].

[3] P. Forn-Díaz, L. Lamata, E. Rico, J. Kono, and E. Solano, Ultrastrong coupling regimes of light-matter interaction, Rev. Mod. Phys. **91**, 025005 (2019).

[4] A. Frisk Kockum, A. Miranowicz, S. De Liberato, S. Savasta, and F. Nori, Ultrastrong coupling between light and matter, Nature Reviews Physics **1**, 19 (2019).

[5] S. Léger, J. Puertas-Martínez, K. Bharadwaj, R. Dassonneville, J. Delaforce, F. Foroughi, V. Milchakov, L. Planat, O. Buisson, C. Naud, W. Hasch-Guichard, S. Florens, I. Snyman, and N. Roch, Observation of quantum many-body effects due to zero point fluctuations in superconducting circuits, Nature Communications **10**, 5259 (2019).

[6] R. Kuzmin, N. Mehta, N. Grabon, R. Mencia, and V. E. Manucharyan, Superstrong coupling in circuit quantum electrodynamics, npj Quantum Information **5**, 20 (2019).

[7] P. Roushan, C. Neill, J. Tangpanitanon, V. M. Bastidas, A. Megrant, R. Barends, Y. Chen, Z. Chen, B. Chiaro, A. Dunsworth, A. Fowler, B. Foxen, M. Giustina, E. Jeffrey, J. Kelly, E. Lucero, J. Mutus, M. Neeley, C. Quintana, D. Sank, A. Vainsencher, J. Wenner, T. White, H. Neven, D. G. Angelakis, and J. Martinis, Spectroscopic signatures of localization with interacting photons in superconducting qubits, Science **358**, 1175 (2017).

[8] R. Ma, B. Saxberg, C. Owens, N. Leung, Y. Lu, J. Simon, and D. I. Schuster, A dissipatively stabilized mott insulator of photons, Nature **566**, 51 (2019).

[9] I. Carusotto, A. A. Houck, A. J. Kollár, P. Roushan, D. I. Schuster, and J. Simon, Photonic materials in cir-

cuit quantum electrodynamics, Nature Physics **16**, 268 (2020).
[10] A. Gyenis, P. S. Mundada, A. Di Paolo, T. M. Hazard, X. You, D. I. Schuster, J. Koch, A. Blais, and A. A. Houck, Experimental realization of a protected superconducting circuit derived from the 0–π qubit, PRX Quantum **2**, 010339 (2021).
[11] A. Gyenis, A. D. Paolo, J. Koch, A. Blais, A. A. Houck, and D. I. Schuster, Moving beyond the transmon: Noise-protected superconducting quantum circuits (2021), arXiv:2106.10296 [quant-ph].
[12] V. E. Manucharyan, *Superinductance*, Ph.D. thesis, Yale University (2012).
[13] I. M. Pop, K. Geerlings, G. Catelani, R. J. Schoelkopf, L. I. Glazman, and M. H. Devoret, Coherent suppression of electromagnetic dissipation due to superconducting quasiparticles, Nature **508**, 369 (2014).
[14] V. E. Manucharyan, J. Koch, L. I. Glazman, and M. H. Devoret, Fluxonium: Single cooper-pair circuit free of charge offsets, Science **326**, 113 (2009).
[15] P. Brooks, A. Kitaev, and J. Preskill, Protected gates for superconducting qubits, Phys. Rev. A **87**, 052306 (2013).
[16] A. Stockklauser, P. Scarlino, J. V. Koski, S. Gasparinetti, C. K. Andersen, C. Reichl, W. Wegscheider, T. Ihn, K. Ensslin, and A. Wallraff, Strong coupling cavity qed with gate-defined double quantum dots enabled by a high impedance resonator, Phys. Rev. X **7**, 011030 (2017).
[17] J. Puertas Martínez, S. Léger, N. Gheeraert, R. Dassonneville, L. Planat, F. Foroughi, Y. Krupko, O. Buisson, C. Naud, W. Hasch-Guichard, S. Florens, I. Snyman, and N. Roch, A tunable josephson platform to explore many-body quantum optics in circuit-qed, npj Quantum Information **5**, 19 (2019).
[18] M. T. Bell, I. A. Sadovskyy, L. B. Ioffe, A. Y. Kitaev, and M. E. Gershenson, Quantum superinductor with tunable nonlinearity, Phys. Rev. Lett. **109**, 137003 (2012).
[19] N. A. Masluk, I. M. Pop, A. Kamal, Z. K. Minev, and M. H. Devoret, Microwave characterization of josephson junction arrays: Implementing a low loss superinductance, Phys. Rev. Lett. **109**, 137002 (2012).
[20] Y. Krupko, V. D. Nguyen, T. Weißl, E. Dumur, J. Puertas, R. Dassonneville, C. Naud, F. W. J. Hekking, D. M. Basko, O. Buisson, N. Roch, and W. Hasch-Guichard, Kerr nonlinearity in a superconducting josephson metamaterial, Phys. Rev. B **98**, 094516 (2018).
[21] L. Grünhaupt, M. Spiecker, D. Gusenkova, N. Maleeva, S. T. Skacel, I. Takmakov, F. Valenti, P. Winkel, H. Rotzinger, W. Wernsdorfer, A. V. Ustinov, and I. M. Pop, Granular aluminium as a superconducting material for high-impedance quantum circuits, Nature Materials **18**, 816 (2019).
[22] A. P. M. Place, L. V. H. Rodgers, P. Mundada, B. M. Smitham, M. Fitzpatrick, Z. Leng, A. Premkumar, J. Bryon, A. Vrajitoarea, S. Sussman, G. Cheng, T. Madhavan, H. K. Babla, X. H. Le, Y. Gang, B. JÃ€ck, A. Gyenis, N. Yao, R. J. Cava, N. P. de Leon, and A. A. Houck, New material platform for superconducting transmon qubits with coherence times exceeding 0.3 milliseconds, Nature Communications **12**, 1779 (2021).
[23] C. Wang, X. Li, H. Xu, Z. Li, J. Wang, Z. Yang, Z. Mi, X. Liang, T. Su, C. Yang, G. Wang, W. Wang, Y. Li, M. Chen, C. Li, K. Linghu, J. Han, Y. Zhang, Y. Feng, Y. Song, T. Ma, J. Zhang, R. Wang, P. Zhao, W. Liu, G. Xue, Y. Jin, and H. Yu, Transmon qubit with relaxation time exceeding 0.5 milliseconds (2021), arXiv:2105.09890 [quant-ph].
[24] K. Makise, R. Sun, H. Terai, and Z. Wang, Fabrication and characterization of epitaxial tin-based josephson junctions for superconducting circuit applications, IEEE Transactions on Applied Superconductivity **25**, 1 (2015).
[25] M. R. Vissers, J. Gao, D. S. Wisbey, D. A. Hite, C. C. Tsuei, A. D. Corcoles, M. Steffen, and D. P. Pappas, Low loss superconducting titanium nitride coplanar waveguide resonators, Applied Physics Letters **97**, 232509 (2010), https://doi.org/10.1063/1.3517252.
[26] H. G. Leduc, B. Bumble, P. K. Day, B. H. Eom, J. Gao, S. Golwala, B. A. Mazin, S. McHugh, A. Merrill, D. C. Moore, O. Noroozian, A. D. Turner, and J. Zmuidzinas, Titanium nitride films for ultrasensitive microresonator detectors, Applied Physics Letters **97**, 102509 (2010), https://doi.org/10.1063/1.3480420.
[27] A. Shearrow, G. Koolstra, S. J. Whiteley, N. Earnest, P. S. Barry, F. J. Heremans, D. D. Awschalom, E. Shirokoff, and D. I. Schuster, Atomic layer deposition of titanium nitride for quantum circuits, Applied Physics Letters **113**, 212601 (2018), https://doi.org/10.1063/1.5053461.
[28] N. Samkharadze, A. Bruno, P. Scarlino, G. Zheng, D. P. DiVincenzo, L. DiCarlo, and L. M. K. Vandersypen, High-kinetic-inductance superconducting nanowire resonators for circuit qed in a magnetic field, Phys. Rev. Applied **5**, 044004 (2016).
[29] D. Niepce, J. Burnett, and J. Bylander, High kinetic inductance NbN nanowire superinductors, Phys. Rev. Applied **11**, 044014 (2019).
[30] C. X. Yu, S. Zihlmann, G. Troncoso Fernández-Bada, J.-L. Thomassin, F. Gustavo, E. Dumur, and R. Maurand, Magnetic field resilient high kinetic inductance superconducting niobium nitride coplanar waveguide resonators, Applied Physics Letters **118**, 054001 (2021), https://doi.org/10.1063/5.0039945.
[31] L. Grünhaupt, N. Maleeva, S. T. Skacel, M. Calvo, F. Levy-Bertrand, A. V. Ustinov, H. Rotzinger, A. Monfardini, G. Catelani, and I. M. Pop, Loss mechanisms and quasiparticle dynamics in superconducting microwave resonators made of thin-film granular aluminum, Phys. Rev. Lett. **121**, 117001 (2018).
[32] W. Zhang, K. Kalashnikov, W.-S. Lu, P. Kamenov, T. DiNapoli, and M. Gershenson, Microresonators fabricated from high-kinetic-inductance aluminum films, Phys. Rev. Applied **11**, 011003 (2019).
[33] O. V. Astafiev, L. B. Ioffe, S. Kafanov, Y. A. Pashkin, K. Y. Arutyunov, D. Shahar, O. Cohen, and J. S. Tsai, Coherent quantum phase slip, Nature **484**, 355 (2012).
[34] O. Dupré, A. Benoît, M. Calvo, A. Catalano, J. Goupy, C. Hoarau, T. Klein, K. L. Calvez, B. Sacépé, A. Monfardini, and F. Levy-Bertrand, Tunable sub-gap radiation detection with superconducting resonators, Superconductor Science and Technology **30**, 045007 (2017).
[35] P. Bonnet, F. Chiodi, D. Flanigan, R. Delagrange, N. Brochu, D. Débarre, and H. le Sueur, Strongly non-linear superconducting silicon resonators (2021), arXiv:2101.11125 [cond-mat.supr-con].
[36] J. Basset, D. Watfa, G. Aiello, M. Féchant, A. Morvan, J. Estéve, J. Gabelli, M. Aprili, R. Weil, A. Kasumov, H. Bouchiat, and R. Deblock, High kinetic inductance microwave resonators made by he-beam assisted deposition of tungsten nanowires, Applied Physics Letters **114**,

102601 (2019), https://doi.org/10.1063/1.5080925.
[37] E. F. C. Driessen, P. C. J. J. Coumou, R. R. Tromp, P. J. de Visser, and T. M. Klapwijk, Strongly disordered tin and nbtin *s*-wave superconductors probed by microwave electrodynamics, Phys. Rev. Lett. **109**, 107003 (2012).
[38] P. C. J. J. Coumou, E. F. C. Driessen, J. Bueno, C. Chapelier, and T. M. Klapwijk, Electrodynamic response and local tunneling spectroscopy of strongly disordered superconducting tin films, Phys. Rev. B **88**, 180505 (2013).
[39] M. Sandberg, M. R. Vissers, J. S. Kline, M. Weides, J. Gao, D. S. Wisbey, and D. P. Pappas, Etch induced microwave losses in titanium nitride superconducting resonators, Applied Physics Letters **100**, 262605 (2012), https://doi.org/10.1063/1.4729623.
[40] T. M. Hazard, A. Gyenis, A. Di Paolo, A. T. Asfaw, S. A. Lyon, A. Blais, and A. A. Houck, Nanowire superinductance fluxonium qubit, Phys. Rev. Lett. **122**, 010504 (2019).
[41] S. Ohya, B. Chiaro, A. Megrant, C. Neill, R. Barends, Y. Chen, J. Kelly, D. Low, J. Mutus, P. J. J. O'Malley, P. Roushan, D. Sank, A. Vainsencher, J. Wenner, T. C. White, Y. Yin, B. D. Schultz, C. J. Palmstrøm, B. A. Mazin, A. N. Cleland, and J. M. Martinis, Room temperature deposition of sputtered TiN films for superconducting coplanar waveguide resonators, Superconductor Science and Technology **27**, 015009 (2013).
[42] S. Verhaverbeke and J. W. Parker, A model for the etching of ti and tin in sc-1 solutions, MRS Proceedings **477**, 447 (1997).
[43] C. E. Murray, Material matters in superconducting qubits (2021), arXiv:2106.05919 [quant-ph].
[44] N. Saveskul, N. Titova, E. Baeva, A. Semenov, A. Lubenchenko, S. Saha, H. Reddy, S. Bogdanov, E. Marinero, V. Shalaev, A. Boltasseva, V. Khrapai, A. Kardakova, and G. Goltsman, Superconductivity behavior in epitaxial tin films points to surface magnetic disorder, Phys. Rev. Applied **12**, 054001 (2019).
[45] A. Torgovkin, S. Chaudhuri, A. Ruhtinas, M. Lahtinen, T. Sajavaara, and I. J. Maasilta, High quality superconducting titanium nitride thin film growth using infrared pulsed laser deposition, Superconductor Science and Technology **31**, 055017 (2018).
[46] B. Sacépé, C. Chapelier, T. I. Baturina, V. M. Vinokur, M. R. Baklanov, and M. Sanquer, Disorder-Induced Inhomogeneities of the Superconducting State Close to the Superconductor-Insulator Transition, Physical Review Letters **101**, 1765 (2008).
[47] Y. Ivry, C.-S. Kim, A. E. Dane, D. De Fazio, A. N. McCaughan, K. A. Sunter, Q. Zhao, and K. K. Berggren, Universal scaling of the critical temperature for thin films near the superconducting-to-insulating transition, Phys. Rev. B **90**, 214515 (2014).
[48] H. K. Kundu, K. R. Amin, J. Jesudasan, P. Raychaudhuri, S. Mukerjee, and A. Bid, Effect of dimensionality on the vortex dynamics in a type-ii superconductor, Phys. Rev. B **100**, 174501 (2019).
[49] M. Faverzani, E. Ferri, A. Giachero, C. Giordano, B. Margesin, R. Mezzena, A. Nucciotti, and A. Puiu, Characterization of the low temperature behavior of thin titanium/titanium nitride multilayer films, Superconductor Science and Technology **33**, 045009 (2020).
[50] S. Probst, F. B. Song, P. A. Bushev, A. V. Ustinov, and M. Weides, Efficient and robust analysis of complex scattering data under noise in microwave resonators, Review of Scientific Instruments **86**, 024706 (2015), https://doi.org/10.1063/1.4907935.
[51] T. Charpentier and et. al., Manuscript under preparation.
[52] C. Müller, J. H. Cole, and J. Lisenfeld, Towards understanding two-level-systems in amorphous solids: insights from quantum circuits, Reports on Progress in Physics **82**, 124501 (2019).
[53] P. K. Day, H. G. LeDuc, B. A. Mazin, A. Vayonakis, and J. Zmuidzinas, A broadband superconducting detector suitable for use in large arrays, Nature **425**, 817 (2003).
[54] F. Henriques, F. Valenti, T. Charpentier, M. Lagoin, C. Gouriou, M. Martínez, L. Cardani, M. Vignati, L. Grünhaupt, D. Gusenkova, J. Ferrero, S. T. Skacel, W. Wernsdorfer, A. V. Ustinov, G. Catelani, O. Sander, and I. M. Pop, Phonon traps reduce the quasiparticle density in superconducting circuits, Applied Physics Letters **115**, 212601 (2019), https://doi.org/10.1063/1.5124967.
[55] L. Cardani, F. Valenti, N. Casali, G. Catelani, T. Charpentier, M. Clemenza, I. Colantoni, A. Cruciani, G. D'Imperio, L. Gironi, L. Grünhaupt, D. Gusenkova, F. Henriques, M. Lagoin, M. Martinez, G. Pettinari, C. Rusconi, O. Sander, C. Tomei, A. V. Ustinov, M. Weber, W. Wernsdorfer, M. Vignati, S. Pirro, and I. M. Pop, Reducing the impact of radioactivity on quantum circuits in a deep-underground facility, Nature Communications **12**, 2733 (2021).
[56] P. Winkel, K. Borisov, L. Grünhaupt, D. Rieger, M. Spiecker, F. Valenti, A. V. Ustinov, W. Wernsdorfer, and I. M. Pop, Implementation of a transmon qubit using superconducting granular aluminum, Phys. Rev. X **10**, 031032 (2020).
[57] C. Wang, C. Axline, Y. Y. Gao, T. Brecht, Y. Chu, L. Frunzio, M. H. Devoret, and R. J. Schoelkopf, Surface participation and dielectric loss in superconducting qubits, Applied Physics Letters **107**, 162601 (2015), https://doi.org/10.1063/1.4934486.
[58] J. Wenner, R. Barends, R. C. Bialczak, Y. Chen, J. Kelly, E. Lucero, M. Mariantoni, A. Megrant, P. J. J. O'Malley, D. Sank, A. Vainsencher, H. Wang, T. C. White, Y. Yin, J. Zhao, A. N. Cleland, and J. M. Martinis, Surface loss simulations of superconducting coplanar waveguide resonators, Applied Physics Letters **99**, 113513 (2011), https://doi.org/10.1063/1.3637047.
[59] G. Calusine, A. Melville, W. Woods, R. Das, C. Stull, V. Bolkhovsky, D. Braje, D. Hover, D. K. Kim, X. Miloshi, D. Rosenberg, A. Sevi, J. L. Yoder, E. Dauler, and W. D. Oliver, Analysis and mitigation of interface losses in trenched superconducting coplanar waveguide resonators, Applied Physics Letters **112**, 062601 (2018), https://doi.org/10.1063/1.5006888.
[60] F. Valenti, F. Henriques, G. Catelani, N. Maleeva, L. Grünhaupt, U. von Lüpke, S. T. Skacel, P. Winkel, A. Bilmes, A. V. Ustinov, J. Goupy, M. Calvo, A. Benoît, F. Levy-Bertrand, A. Monfardini, and I. M. Pop, Interplay between kinetic inductance, nonlinearity, and quasiparticle dynamics in granular aluminum microwave kinetic inductance detectors, Phys. Rev. Applied **11**, 054087 (2019).
[61] R. Barends, J. Wenner, M. Lenander, Y. Chen, R. C. Bialczak, J. Kelly, E. Lucero, P. O'Malley, M. Mariantoni, D. Sank, H. Wang, T. C. White,

Y. Yin, J. Zhao, A. N. Cleland, J. M. Martinis, and J. J. A. Baselmans, Minimizing quasiparticle generation from stray infrared light in superconducting quantum circuits, Applied Physics Letters **99**, 113507 (2011), https://doi.org/10.1063/1.3638063.

[62] J. Gao, J. Zmuidzinas, A. Vayonakis, P. Day, B. Mazin, and H. Leduc, Equivalence of the effects on the complex conductivity of superconductor due to temperature change and external pair breaking, Journal of Low Temperature Physics **151**, 557 (2008).

[63] U. S. Pracht, N. Bachar, L. Benfatto, G. Deutscher, E. Farber, M. Dressel, and M. Scheffler, Enhanced cooper pairing versus suppressed phase coherence shaping the superconducting dome in coupled aluminum nanograins, Phys. Rev. B **93**, 100503 (2016).

[64] P. B. Dieterle, M. Kalaee, J. M. Fink, and O. Painter, Superconducting cavity electromechanics on a silicon-on-insulator platform, Phys. Rev. Applied **6**, 014013 (2016).

[65] A. Melville, G. Calusine, W. Woods, K. Serniak, E. Golden, B. M. Niedzielski, D. K. Kim, A. Sevi, J. L. Yoder, E. A. Dauler, and W. D. Oliver, Comparison of dielectric loss in titanium nitride and aluminum superconducting resonators, Applied Physics Letters **117**, 124004 (2020), https://doi.org/10.1063/5.0021950.

[66] M. Tinkham, *Introduction to Superconductivity*, 2nd ed. (Courier Corporation, 2004).

[67] M. Pita-Vidal, A. Bargerbos, C.-K. Yang, D. J. van Woerkom, W. Pfaff, N. Haider, P. Krogstrup, L. P. Kouwenhoven, G. de Lange, and A. Kou, Gate-tunable field-compatible fluxonium, Phys. Rev. Applied **14**, 064038 (2020).

[68] T. Brecht, M. Reagor, Y. Chu, W. Pfaff, C. Wang, L. Frunzio, M. H. Devoret, and R. J. Schoelkopf, Demonstration of superconducting micromachined cavities, Applied Physics Letters **107**, 192603 (2015), https://doi.org/10.1063/1.4935541.